PICOSEC Micromegas

GDD
Gas Detectors Development Group

PICOSEC Micromegas Gaseous Detector for Precise Timing in High-Rate Environment

M. L. Velázquez Fernández[1, 2], F. Brunbauer[2] and M. Lisowska[2]
On behalf of EP-DT-DD Gaseous Detector Development (GDD) team.

[1]*School of Physics and Astronomy, University of Edinburgh, Edinburgh EH9 3FD, UK*
[2]*European Organization for Nuclear Research (CERN), Geneva, Switzerland*

August 30, 2024

Abstract

As experiments advance toward higher luminosities and more demanding physics, precise timing detectors become increasingly essential. The PICOSEC Micromegas (MM), a novel gaseous detector concept, offers a timing resolution in the order of tens of picoseconds, significantly improving over traditional Micromegas detectors.

This study evaluates the performance of various PICOSEC MM configurations, including single-pad detectors with different mesh types, medium granularity pads, and double Diamond-Like Carbon (DLC) MM. The gain, spatial resolution, and time resolution were measured in laboratory tests with an Ultraviolet (UV) LED and during a test beam campaign at CERN-SPS-H4.

Results indicate that the standard mesh provides the best gain and time resolution. In contrast, the electroformed and thin woven meshes exhibited reduced field uniformity and transparency, with the latter being confirmated by simulations. Medium granularity pads achieved a spatial resolution of 1.8 mm and a time resolution of $\sim$43 ps. Lastly, the double DLC MM amplitude uniformity was measured, resulting in a mean amplitude of about 15 mV and a coefficient of variation of 8%.

Keywords: PICOSEC, Micromegas, Gaseous Detectors, Time Resolution, Gain, Spatial Resolution, UV LED, CERN-SPS-H4, COMSOL MultiPhysics, Garfield++.

Contents

1 Introduction **3**
1.1 PICOSEC Micromegas Detector 3
1.2 Theoretical Background on Waveform Analysis 4

2 Characterisation of micromeshes using single-pad detectors **7**
2.1 Meshes transparency analysis 8
2.2 SPE Analysis and Results 10
2.3 Test Beam Analysis and Results 12

3 Characterisation of position reconstruction using a medium granularity detector **14**
3.1 Signal amplitude 15
3.2 Space resolution 17
3.3 Time resolution 18

4 Double DLC Multipad **20**

5 Conclusion **22**

Acknowledgements **22**

Appendix **25**
COMSOL Simulation 25
Signal extraction and theoretical PE spectra 26

1 Introduction

Gaseous detectors have been essential in particle physics due to their ability to precisely track charged particles and measure their energy. They are also cost-effective and robust in high-radiation environments, especially over large areas. Thus, their advantages over other detector technologies include reliability, scalability, and durability [1].

The evolution of gaseous detectors began in the early 20th century with the development of Geiger-Müller and proportional counters [2][3], which first demonstrated the effectiveness of ionized gas for radiation detection [1]. In the late 1980s, the Micro-Strip Gas Chamber (MSGC) emerged, using microfabrication techniques to enhance spatial resolution and rate capability [4]. Building on these advancements, a major leap was made in 1996 with the introduction of the MicroMegas (Micro-Mesh Gaseous Structure) detectors by Georges Charpak and Ioannis Giomataris [5]. These detectors improved upon wire chamber technology by employing a fine micromesh to separate the drift and amplification regions, enabling efficient electron multiplication. Typically, in a MM detector, a high electric field is established between a micromesh and an anode, separated by a uniform gap of approximately 128 µm, maintained by pillars that are photolithographically structured. MM technology has since been widely adopted, notably in the ATLAS New Small Wheel upgrade at the Large Hadron Collider (LHC) [6].

Despite the established use of MM gaseous detectors in large-scale tracking systems, including LHC experiments, the time resolution of conventional MM detectors is constrained by uncertainties in the primary ionisation location within the sensitive detection volumes, which are typically several millimetres thick [5]. Due to the low density of the gaseous medium, reducing the thickness of these ionisation volumes to enhance timing precision is not feasible, as the gap will not be sufficient for an effective ionisation of the volume, resulting in a timing jitter generally confined to the nanosecond range [7].

Recent advancements, such as the PICOSEC detector, have significantly improved time resolution to approximately 25 picoseconds, providing a scalable solution with excellent timing precision [8][9].

1.1 PICOSEC Micromegas Detector

The PICOSEC Micromegas detector introduces a novel approach to enhance timing precision by integrating a Cherenkov radiator, which emits prompt Cherenkov light as particles pass through. This light is immediately converted into photoelectrons (PE) by a semi-transparent photocathode layer directly coated onto the surface of the radiator crystal. The essential innovation of PICOSEC lies in the precise and synchronous generation of these PE at a well-defined location, significantly reducing timing uncertainty [7][10].

As illustrated in Figure 1, the PE produced by the Cherenkov light when hitting the photocathode enter into a gas-filled region (Ne[80%]:CF_4[10%]:C_2H_6[10%]) at ambient pressure [7]. There, they encounter a high electric field generated between the photocathode, a micromesh, and the anode. The field accelerates the electrons, causing them to collide with gas molecules, producing additional electrons — a process known as avalanche multiplication.

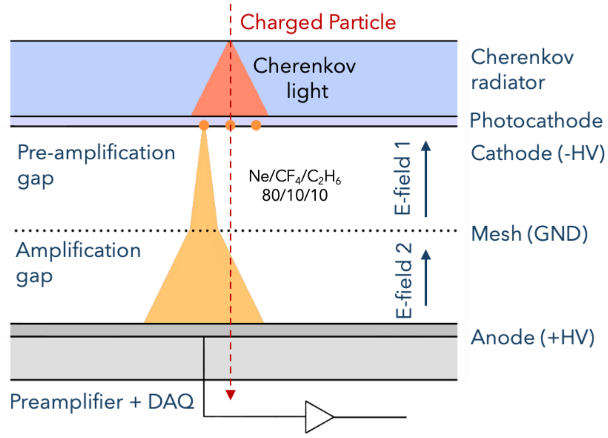

Figure 1: Schematic representation of the PICOSEC Micromegas detector working principle.

1.2 Theoretical Background on Waveform Analysis

A typical waveform produced in a PICOSEC detector features an electron peak followed by an ion tail, as depicted in Figure 2a. The electron peak corresponds to the induced signal in the anode as the electrons rapidly traverse the amplification region. On the contrary, the ion tail arises from the slower drift of ions, which are significantly heavier than electrons by several orders of magnitude. It is important to note that the signals induced by the motion of the electrons or ions are only visible in the amplification region. This is due to the effective screening provided by the micromesh kept at ground potential.

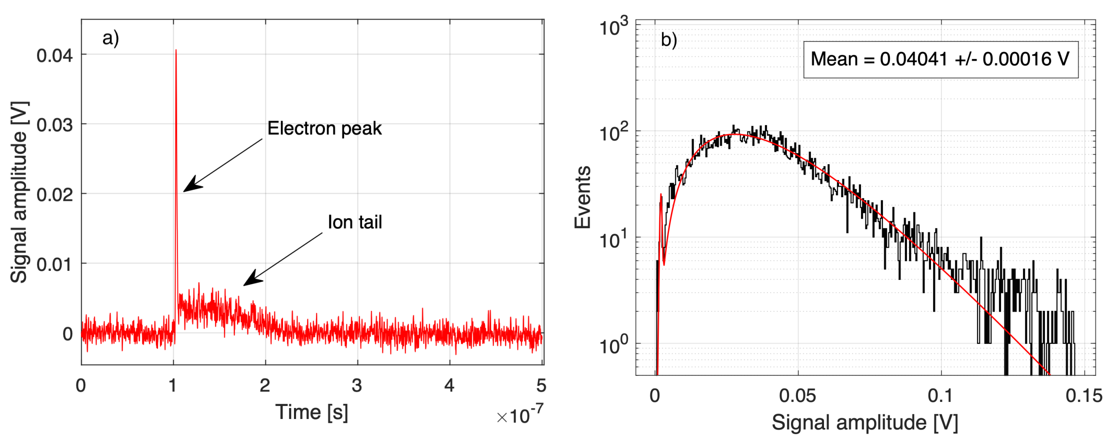

Figure 2: a) Example of a waveform obtained from the PICOSEC detector. b) Single photoelectron amplitude spectra, with the corresponding Polya fit of the spectra and Gaussian noise fit.

The signal amplitudes in a PICOSEC detector follow a probability density function described by a Polya distribution:

$$A(Q|N, Q_e, \theta) = \frac{(\theta+1)^{N(\theta+1)}}{\Gamma(N(\theta+1))} \left(\frac{Q}{Q_e}\right)^{N(\theta+1)-1} \exp\left(-(\theta+1)\frac{Q}{Q_e}\right), \tag{1}$$

where Q_e is the mean charge per photoelectron, N is the number of photoelectrons, and θ is the Polya shape parameter [9].

The mean of this distribution represents the average signal charge of the PICOSEC-Micromegas, which is essential for calculating the detector's gain. The gain is determined by dividing the mean signal charge $\langle Q \rangle$ from a single photoelectron by the product of the amplifier gain and the electron charge e [11].

In waveform analysis, the electron-peak charge is determined by integrating the waveform from its start to the endpoint. These points are identified as the first positions before and after the peak where the amplitude falls within one standard deviation of the baseline offset. For cases where the electron peak and ion tail are not distinguishable, the endpoint is defined as the moment when the pulse derivative changes sign [9]. Therefore, to improve the signal integration, a charge-sensitive preamplifier is used to measure the signal amplitude.

In low signal scenarios, where the signal-to-noise ratio (SNR) is low, a noise peak appears in the spectra at low amplitudes (in the order of mV), which can be parametrised by a Gaussian distribution. The combination of the Polya distribution for the signal and the Gaussian for the noise effectively characterises the overall signal spectrum, as shown in Figure 2b.

The next step in analysing the performance of the PICOSEC detector involves obtaining the time resolution from the waveform. This is achieved by fitting a sigmoid function to the leading edge of the electron peak (example presented in Figure 3), defined as:

$$f(t) = P_3 + \frac{P_0}{1 + \exp\left(\frac{P_1 - t}{P_2}\right)}, \tag{2}$$

where P_0 and P_3 represent the maximum and minimum values of the sigmoid, P_1, is the inflexion time (i.e., the point where the slope changes its rate of change), and P_2 quantifies the steepness of the sigmoid (i.e., it is correlated to the signal rise time) [9]. The time corresponding to a 20% constant fraction (CF) of the signal is calculated as follows [9]:

$$t_{CF} = P_1 - \frac{1}{P_2} \cdot ln(\frac{P0}{0.2 \times V_{max} - P_3} - 1). \tag{3}$$

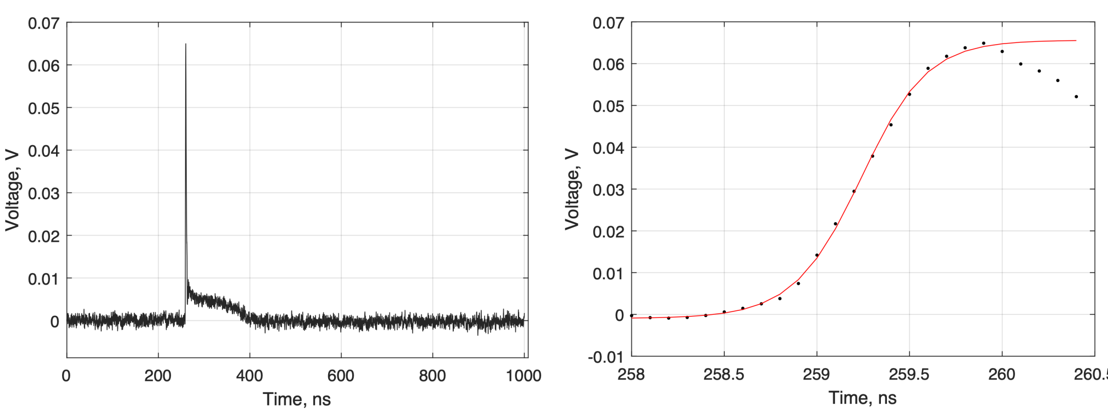

Figure 3: Left: example of a waveform obtained with the PICOSEC detector. Right: sigmoid fit to the rising edge of the signal.

After calculating the CF for the reference detector — a detector with well-known and stable characteristics — and the Device Under Test (DUT), the Signal Arrival Time (SAT) is defined as the difference between the timestamps of both detectors.

In addition, to correct for the time walk effect, the SAT as a function of the signal amplitude is fitted with a power-law model (Figure 4) given by,

$$f(x) = a + \frac{b}{x^c} \tag{4}$$

where a, b, and c are variable parameters, and x, is the independent variable (in this case, the energy peak). Subtracting the time walk correction from the data, the time resolution is obtained from the residuals of the corrected SAT.

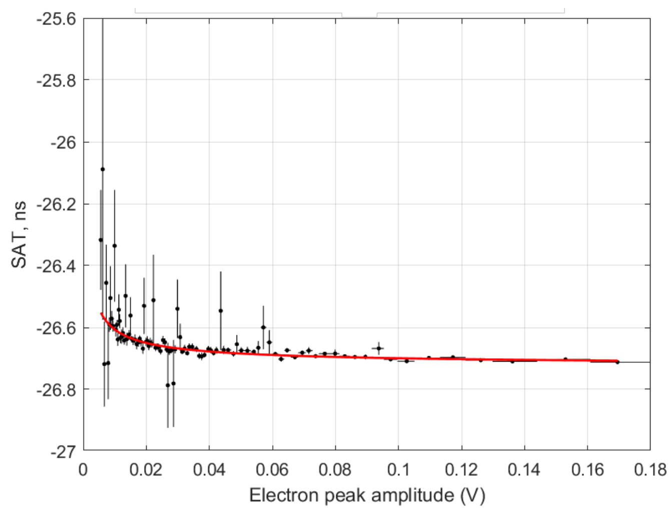

Figure 4: Signal arrival time (SAT) as a function of the electron peak amplitude, where the red fit line represents the time walk correction.

With this information in hand, the performance of various PICOSEC Micromegas configurations was examined. The analysis covered the following prototypes: single pads with varying mesh types (Section 2), medium granularity pads (Section 3), and double DLC (Diamond-Like Carbon) Micromegas (Section 4).

2 Characterisation of micromeshes using single-pad detectors

Single pad detectors represent the simplest configuration of the PICOSEC MM detector and are primarily used to investigate its main features, such as gain, spatial resolution, and time resolution.

These detectors are housed within an aluminium case, designed with a sandwich-like structure that simplifies the assembly of different prototypes. The various layers of this configuration are illustrated in Figure 5. The main components are a quartz window that encloses the gas volume; the PEEK insert to provide structural support for the other components; the Cherenkov radiator, constructed from MgF_2 with a thickness of 3 mm, features a photocathode, such as CsI, DLC, or chromium, coated on its surface; a spacer to determine the boundaries of the preamplification gap; and the MM board, containing the micromesh and providing connection to the readout electronics [12]. The detector is operated at a atmospheric pressure [7], either in a sealed or flushing mode.

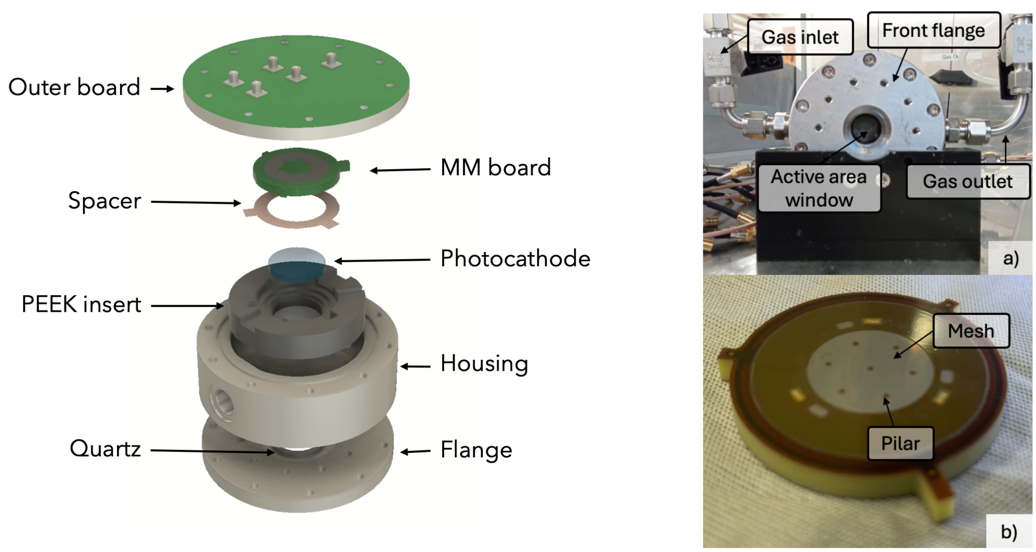

Figure 5: On the left, a schematic representation of the single pad detector. On the right, a) a close-up of the MM board; b) a front view of the detector.

For the scope of this project, the characterisation of three different MM boards equipped with three different photolithography meshes has been performed. These are a standard woven mesh (STD) [Hole width: 45 µm, wire width: 18 µm], an electroformed mesh (EF) [Hole: 30 µm, wire: 20 µm], and a thin woven mesh (Thin) [Hole: 20 µm, wire: 15 µm], illustrated in Figure 6.

So far, the standard mesh has been used for the majority of PICOSEC prototypes. The motivation for testing the EF or thin mesh is to evaluate the performance in a hypothetically more uniform electric field and thus higher gain. However, concerns were raised about the lower transparency of these two meshes and the uniformity of the field in the EF mesh, as there were visible wrinkles on the surface, coming from limitations on stretching force during the manufacturing process.

The rest of this section focuses on characterising the single pad detectors, including the gain, space resolution, and time resolution. Analysis was performed both in the GDD laboratory using a UV LED for the characterisation of the detector under single photoelectron (SPE) responses (Section 2.2) and on the CERN-SPS-H4 beam line using 150 GeV/c muons for the time resolution characterisation (Section 2.3). In addition, simulations have been conducted to understand the detector properties.

2.1 Meshes transparency analysis

As a preliminary evaluation of the transparency, the dimensions of each of the meshes, and the images retrieved using the optical microscope were analysed using the ImageJ software (Table 1) [13]. By defining the transparency as the percentage of electrons that would reach the amplification region when probed perpendicular to the mesh under the effect of no electric field, the transparency would be equivalent to the open area of the mesh. With this definition, the standard mesh with an open area of 49(2)% would be the one with the highest transparency, followed by the electroformed mesh with 37(2)%, and the thin woven mesh with an open area of 32(2)%.

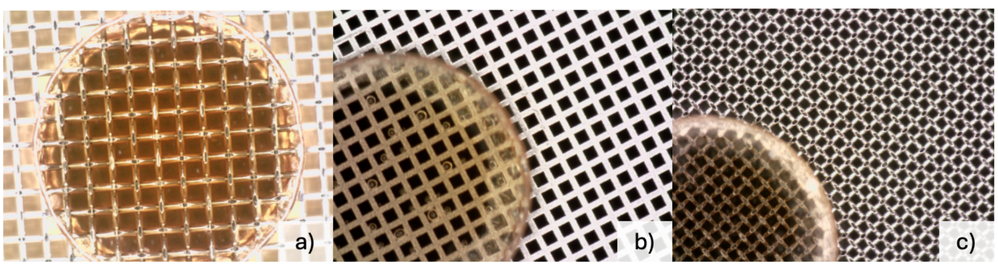

Figure 6: Pictures of the different meshes under the optical microscope. a) standard woven mesh, b) electroformed mesh, c) thin woven mesh. The circular patterns observed correspond to the solder mask pillars.

Mesh	**Hole diameter** [µm]	**Wire diameter** [µm]	**Open area** [%]
STD	44.0(1.1)	19.0(7)	49(2)
EF	30.4(6)	19.6(7)	37(2)
Thin	19.9.(9)	15.1(4)	32(2)

Table 1: Characterisation of the different meshes used in the single pad detectors.

Nevertheless, a lower transparency value is anticipated in contrast to standard MM operation. In standard MM, the field applied in the drift region is much smaller than in the amplification region. However, in the PICOSEC system, the field ratio between the preamplification and amplification gaps is approximately 2:1 (cathode: about 500 V, anode: about 275 V). This configuration accelerates the electrons in a manner that prevents them from focusing along the field lines and instead, some of them being collected by the mesh. To better assess the transparency, simulations were conducted.

The simulation utilized COMSOL MultiPhysics [14] for finite element analysis of the electric field within the detector (refer to the Appendix), Garfield++ [15] for modelling electron transport in the gas volume, and Magboltz [16] for calculating the electron drift velocity and Townsend coefficient specific to the detector's gas mixture. For a visual representation of the electron drift lines within the detector refer to Figure 7.

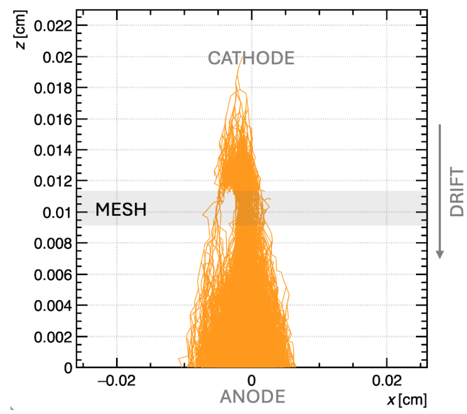

Figure 7: Simulated drift lines of the electrons within a PICOSEC detector operated at 275 V on the anode and 500 V on the cathode.

To determine the mesh transparency, the `AvalancheMicroscopic` class in Garfield++ was modified to include the `CrossingSection` function. This function calculates the ratio of electrons moving from an initial to a final z-position. Thus, by defining transparency as the ratio of the electrons at the top of the mesh to those that reach the amplification region, the transparency of the different meshes was obtained, by stochastically generating the primary electrons over the projection of the pitch on the photocathode. This resulted in a transparency over the mesh of 12(9)% for the STD mesh, 4.0(16)% for the Thin mesh, and 9(3)% for the EF mesh, as seen in Figure 8. As a side note, this simulation was conducted using 275 V on the anode and 500 V on the cathode.

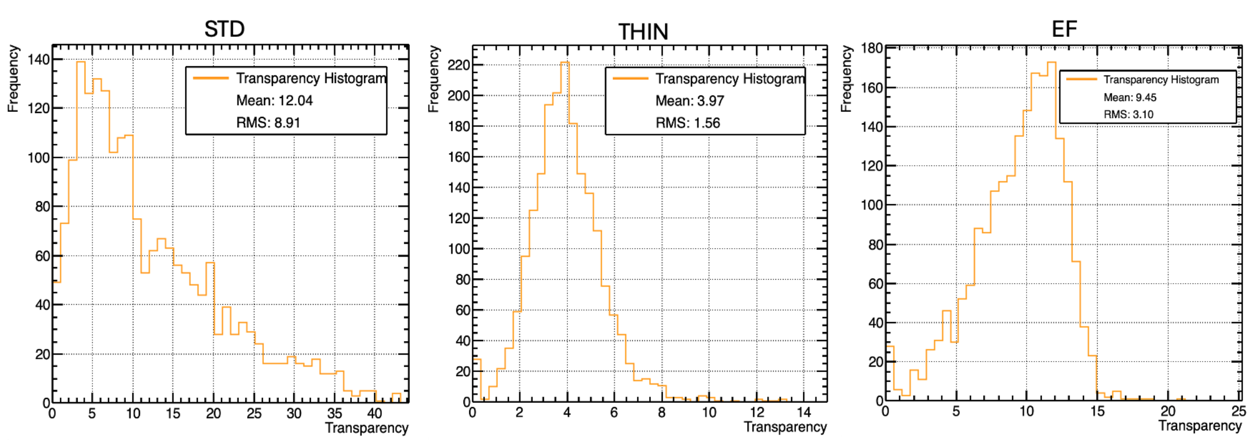

Figure 8: Overall transparency distribution of the different meshes: standard mesh, thin woven mesh and electroformed mesh.

Additionally, to achieve a more detailed characterization, primary electrons were probed at specific fixed positions: 1) At the centre of the pitch; 2) at the centre of a wire; 3) at the intersection of wires; 4) halfway across the pitch; and 5) at the centre of a quadrant of the mesh hole. The result of the transparency at each location is showcased in table 2. Refer to Figure 9 for a visual representation.

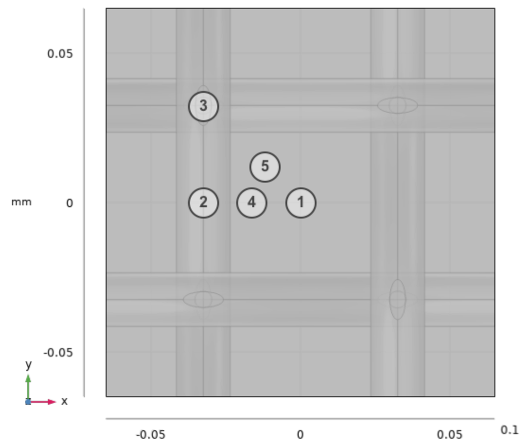

Figure 9: Schematic representation of the mesh transparency mapping points, exemplified with the STD mesh.

Mesh	Transparency [%]				
	Point 1	**Point 2**	**Point 3**	**Point 4**	**Point 5**
STD	28.3	8.08	2.12	18.5	17.4
EF	12.23	8.11	5.48	11.15	11.16
Thin	3.24	2.1	1.41	2.98	3.01

Table 2: Transparency of different meshes for primary electrons at the specified points in the text. The simulation for obtaining these values used 275 V on the anode and 500 V on the cathode.

In contrast, when defining transparency as the ratio of the number of electrons just before the mesh to those that reach the amplification region, electron multiplication in the mesh region is taken into account. Based on this definition, the estimated results for the different meshes are 35(8)% for the STD mesh, 15(8)% for the EF mesh, and 3.8(13)% for the Thin mesh.

Given this information, the performance of the different geometries was evaluated to determine the best configuration for the PICOSEC detector and to understand the limitations that transparency could impose on the detector.

2.2 SPE Analysis and Results

Single photoelectron (SPE) response was studied at the Gaseous Detectors Development (GDD) laboratory using a UV LED as the light source and a Chromium photocathode. The detector signals were amplified using a charge-sensitive preamplifier and recorded with a LECROY WaveRunner 8104 oscilloscope [17]. An example of a waveform obtained under these conditions is shown in Figure 10.

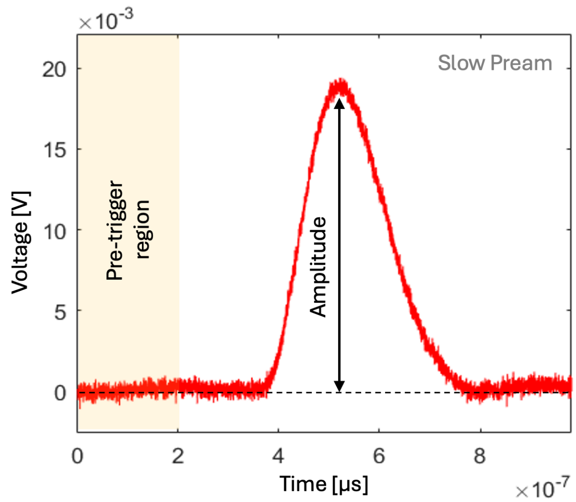

Figure 10: Example of a waveform obtained from the PICOSEC detector using a slow preamplifier. The shaded area represents the pretrigger region used to measure the noise baseline.

Data collection spanned from the lowest voltages at which signals exceeded the noise level to the highest stable voltage for a given anode setting. For each voltage configuration, approximately 20,000 signals were sampled and analysed. The amplitude spectra were fitted using the Polya function, as defined in equation 1 and explained previously.

The mean SPE amplitude was plotted as a function of the cathode voltage, revealing that the detector's gain is significantly influenced by the mesh transparency, as hypothesised. As observed in Figure 11, the STD mesh exhibits the highest gain, followed by the electroformed mesh and the thin woven mesh. The maximum achievable amplitude is around 40 mV, indicating that avalanches generating larger signals might approach the Raether limit [18]. At this point, the ionization of the gas could create conductive paths within the detector, potentially leading to sparking and instabilities.

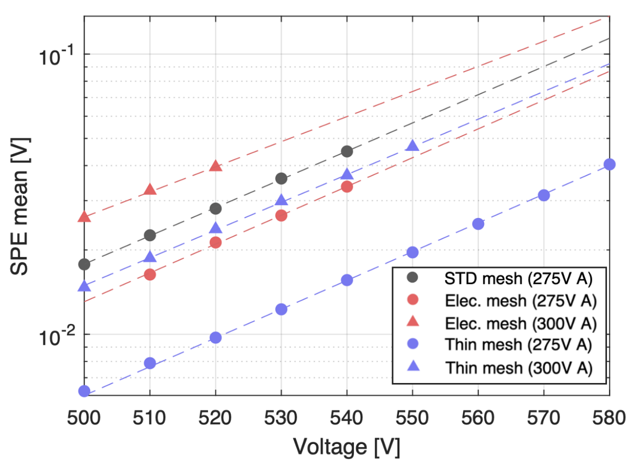

Figure 11: Mean SPE amplitude as a function of the cathode voltage for different meshes at 275 V on the anode.

2.3 Test Beam Analysis and Results

The signal amplitude and time resolution of the detectors were measured at the CERN-SPS-H4 beam line with 150 GeV/c muons during a DRD1 test beam campaign, using CsI photocathodes and operating in flushing mode because of the quick degradation of the gas quality.

A telescope comprising three tracking Gaseous Electron Multipliers (GEMs) detectors with two-dimensional strip readout was used to reconstruct the trajectory of each muon using a combinatorial Kalman filter-based algorithm [19], which also determined its impact position on each detector. Additionally, the setup included a Micro-Channel Plate Photomultiplier Tube (MCP-PMT, Hamamatsu R3809U-50 [20], with a time resolution of ∼8 ps not substracted in the following analysis) that served as a reference detector and provided a trigger signal for the DAQ system. The telescope was equipped with six movable stages for positioning the Devices Under Test (DUTs). The layout of the test beam setup is shown in Figure 12.

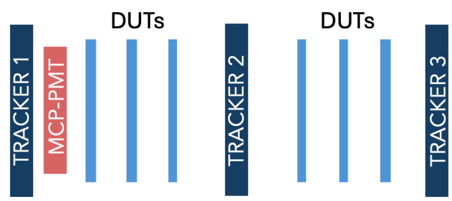

Figure 12: Layout of the test beam setup. The tracker detectors consist of triple-GEMs, with an MCP-PMT serving as the trigger and reference detector. DUT stands for Device Under Test.

Signal amplitudes were measured following the same procedure as in the laboratory, although a fast preamplifier was used in this case to facilitate time resolution measurements. The mean amplitudes obtained mirrored the trends observed in the lab, with the STD mesh achieving the highest gain for a given anode voltage. Despite lower statistics for the STD mesh, due to prior testing in other campaigns, the results suggest that increasing the anode voltage would yield higher amplitudes at lower cathode voltages. Be that as it may, the STD mesh produced the best results, with a mean amplitude of 174.2(8) mV at 275 V on the anode and 440 V on the cathode, as shown in Figure 13.

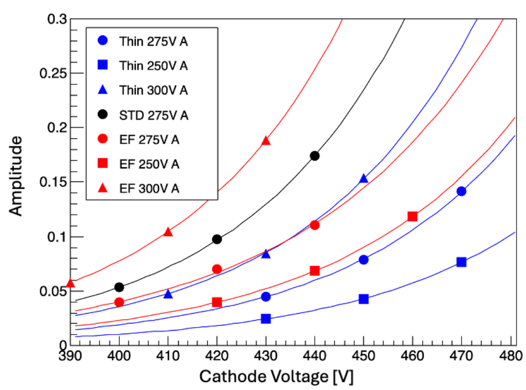

Figure 13: Amplitude of the signal as a function of cathode voltage for different meshes and anode voltages.

The time resolution was determined by comparing the arrival time of the beam particles, as measured by the MCP-PMT, with the signal arrival time recorded by the PICOSEC detector, as described in section 1.2.

Similar to the amplitude analysis, time resolution was evaluated as a function of the cathode voltage for different meshes and anode voltages (Figure 15). The best time resolution was achieved by the standard mesh at 275 V on the anode and 440 V on the cathode, reaching 19.4 ps, as shown in Figure 14.

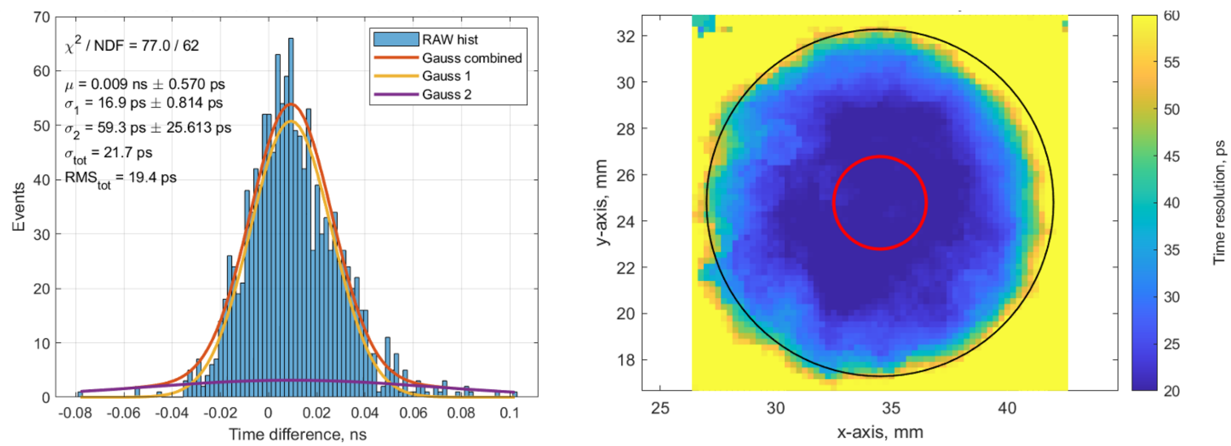

Figure 14: The left plot illustrated the time resolution for the standard mesh operated at 275 V on the anode and 440 V on the cathode. The right plot shows a time resolution map across the detector's active area.

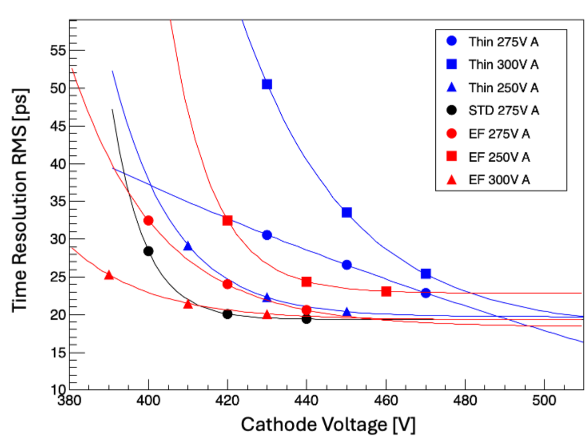

Figure 15: Time resolution as a function of cathode voltage for different meshes and anode voltages.

Therefore, after all the characterisations conducted, the STD mesh is the one that provides the best results in terms of gain and time resolution. The limiting factor of the detector has been confirmed to be the transparency of the mesh and uniformity of the field which in the case of the electroformed mesh is limited by the manufacturing process.

3 Characterisation of position reconstruction using a medium granularity detector

The medium granularity detector is a 2D pad detector with a 15 mm diameter active area, featuring nineteen hexagonal pads with a 3.5 mm pitch, as illustrated in Figure 16. This design aims to improve spatial resolution while maintaining the time resolution of the PICOSEC detector. This classification of "medium granularity" contrasts with a higher granularity version that uses a 2.2 mm pad pitch, which has not yet been tested.

Each pad on the MM board is connected to the outer Printed Circuit Board (PCB) using pogo-pins, which are linked to the corresponding amplifiers. In this setup, data was recorded using the SAMPIC waveform TDC digitiser [21] instead of an oscilloscope. The detector data was collected at the CERN-SPS-H4 beam line using 150 GeV/c muons, with the aid of the telescope described in the previous section.

However, the data collected during this beam campaign was constrained by connectivity issues affecting many runs. Only one run provided relatively good area coverage, allowing observation of fully contained events, although Pads 9, 16, and 17 were disconnected. Refer to Figure 17 for details.

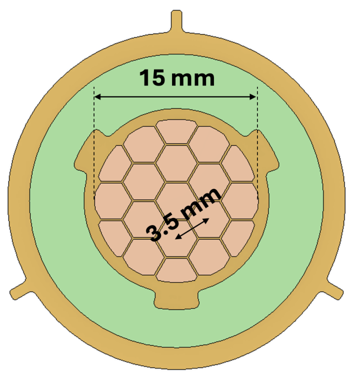

Figure 16: Schematic diagram of the medium granularity MM board.

For the analysis, it was considered that the signal from the incoming particle is distributed across multiple pads. This occurs because the initial Cherenkov cone spreads across a 6 mm diameter circle, allowing photoelectrons to be generated over this area. Consequently, the drifting electrons are detected by different pads. The number of pads registering the signal is referred to as the pad multiplicity, and as shown in Figure 17, most events are shared between three pads.

To merge the information belonging to an event together, channels are grouped based on the temporal alignment of their signals. Each signal is timestamped, and those with similar timestamps are considered part of the same event. A reference channel is used to benchmark time differences, with channels showing minimal time differences relative to this reference being grouped together.

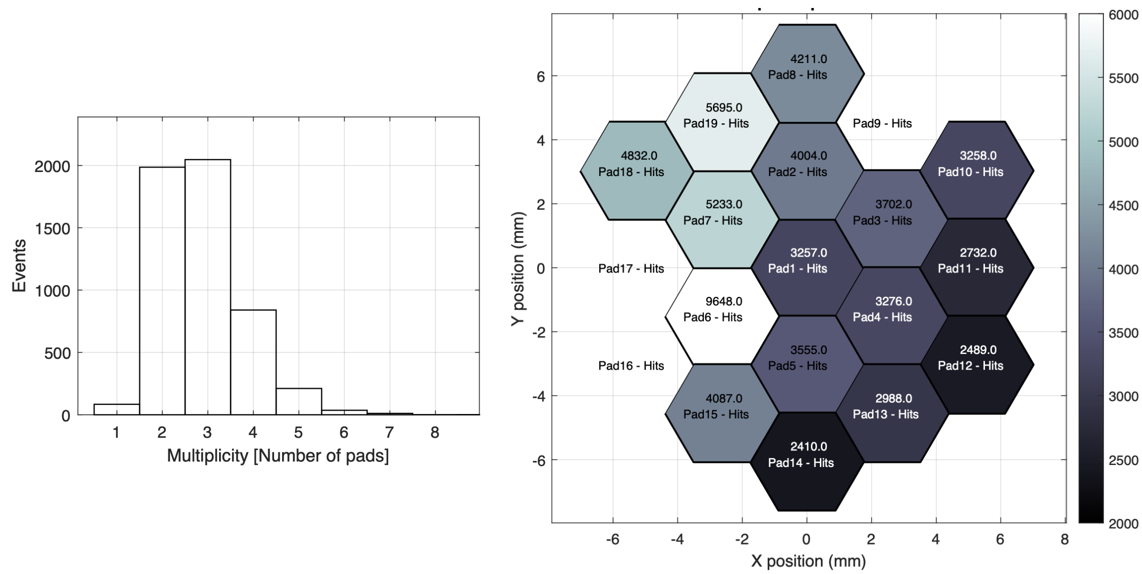

Figure 17: Left: histogram of the multiplicity of events per pad for the medium granularity detector. Right: map of the registered waveforms per pad. Note that the outer pads are in reality not a fully hexagonal shape.

The following sections will discuss in more detail the analysis performed to optimise the time resolution of the detector (Section 3.3), the signal amplitude (Section 3.1), and the space resolution (Section 3.2).

3.1 Signal amplitude

Initially, the waveforms from the active pads were analyzed individually. The signal spectra for each pad were fitted using the Polya function, as discussed in the previous section. The resulting amplitude distribution for each pad is presented in Figure 18.

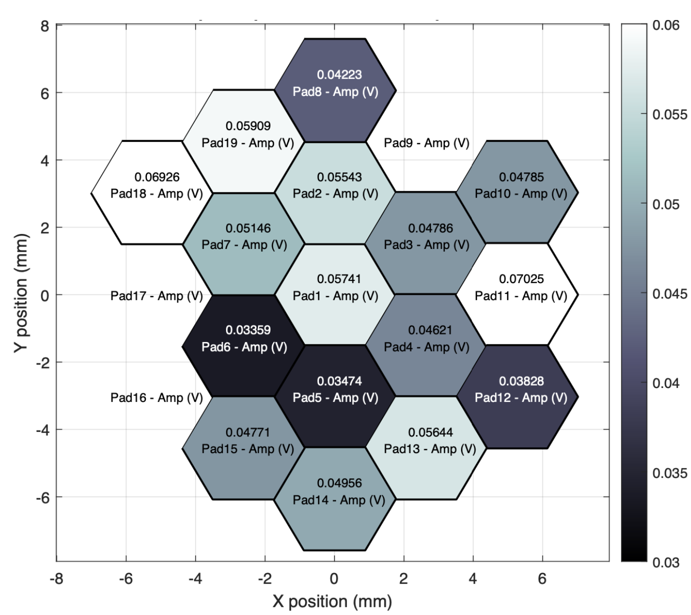

Figure 18: Amplitude distribution of the signal for each pad of the medium granularity detector.

Subsequently, the partial signals from the active pads were summed to characterize the total energy of each event. The combined amplitude distribution for full events is shown in Figure 19.

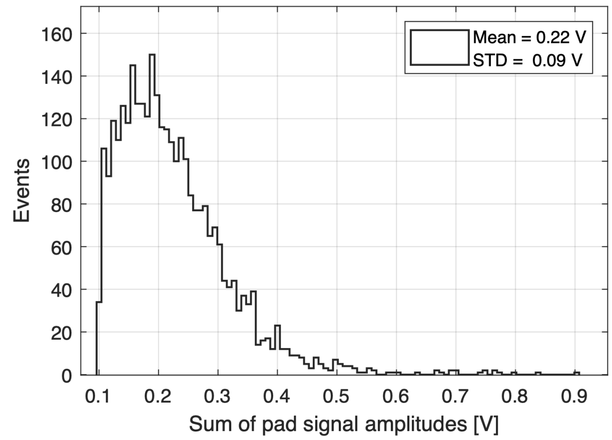

Figure 19: Amplitude spectrum for the combined signals of the active pads (full event).

Using these results, the fraction of primary photoelectrons contributing to the signal on each pad was determined. The total amplitude of the electron signal was plotted against the leading pad (the pad with the highest signal amplitude), the second leading pad, and the third leading pad, as these pads provided sufficient statistics for analysis (refer again to Figure 17). The gradient of the least-squares fit to the data corresponds to the percentage of photoelectrons that induced the signal on each pad.

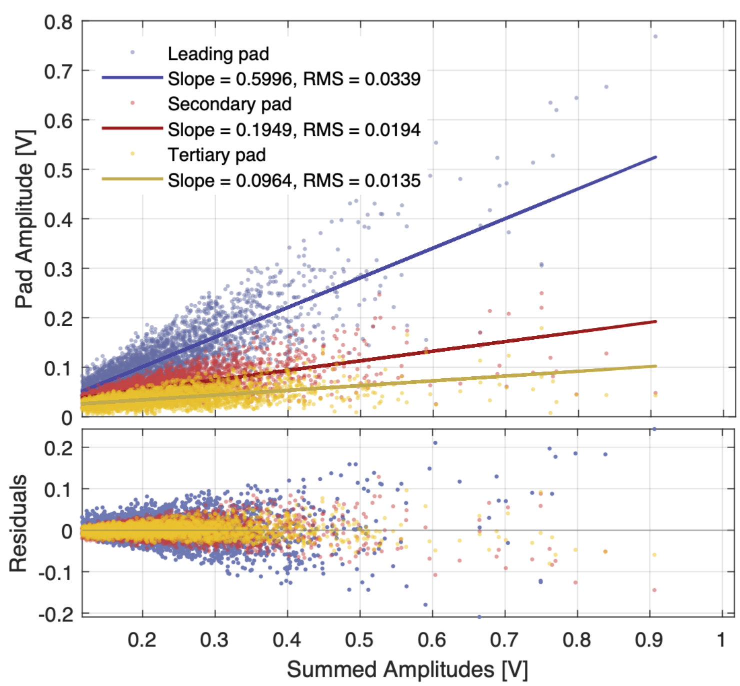

Figure 20: Distribution of photoelectrons across the leading pads of the medium granularity detector.

As illustrated in Figure 20, the leading pad captured 60(3)% of the total signal, the second leading pad accounted for 19(2)%, and the third leading pad recorded 9.6(14)%. The uncertainties are derived from the root mean square (RMS) of the residuals of the fit.

3.2 Space resolution

Position reconstruction was performed using a weighted average approach based on the signal amplitudes from the active pads, given by the formula,

$$X_{\text{reco}} = \sum_{i=1}^{N} \frac{X_i \cdot A_i}{\sum_{j=1}^{N} A_j} \tag{5}$$

where X_{reco} is the reconstructed position, X_i is the position of pad i, A_i is the signal amplitude in pad i, and N is the number of active pads. The position reconstruction was performed for each event, and the residuals were calculated by comparing the reconstructed position with the tracked position obtained from the telescope. For ease of visualisation, two examples of the position reconstruction are shown in Figure 21.

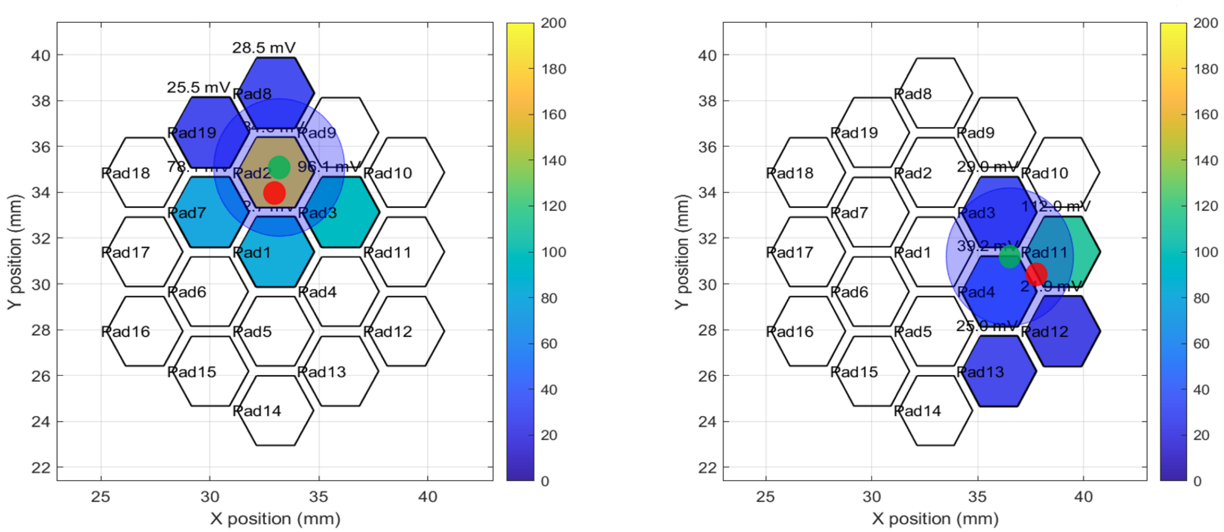

Figure 21: Position reconstruction example for the medium granularity detector. The green dot indicates the tracked position by the telescope, while the red dot represents the reconstructed position. The shaded area around the tracked position shows the projection of the Cherenkov cone on the photocathode.

The position reconstruction resolution was quantified by fitting a Gaussian function to the residuals of the reconstructed positions. The standard deviation of the Gaussian provided the position resolution of the detector, which was found to be 1.31 mm in the x-direction and 1.25 mm in the y-direction, as illustrated in Figure 22. Therefore, the overall space resolution of the medium granularity detector was determined to be 1.8 mm.

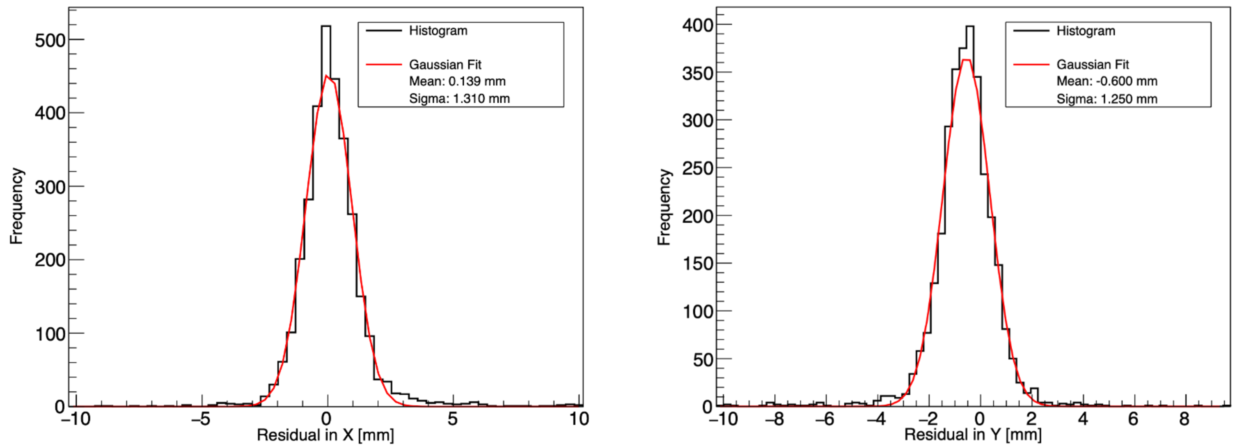

Figure 22: Residuals of the reconstructed positions for the medium granularity detector, shown separately for the x-axis (left) and y-axis (right).

3.3 Time resolution

To analyze the time resolution of the detector, two approaches were employed. The first approach involved examining the raw waveform from each pad independently, without combining waveforms from the same event. The second approach involved merging waveforms corresponding to the same event to determine the overall time resolution of the detector.

For individual pads, the time resolution was determined using the analysis method described in Section 1.2. This yielded time resolutions ranging from 30 ps to 60 ps, as shown in Figure 23.

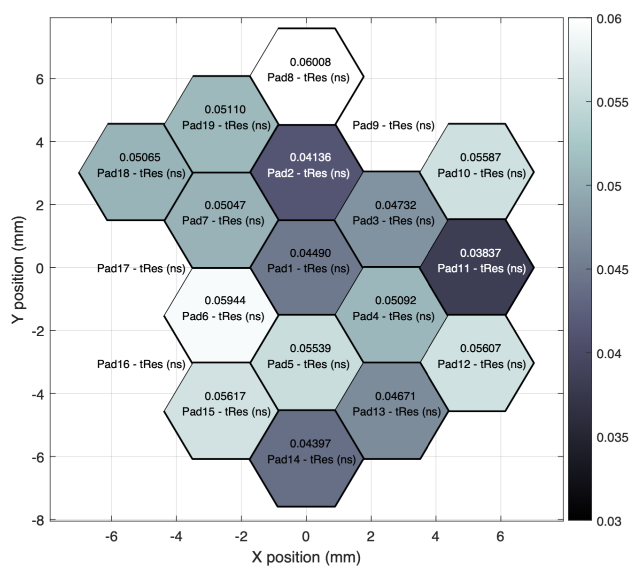

Figure 23: Time resolution per pad for the medium granularity detector.

To obtain the combined time resolution of the detector, it was necessary to consider time walk and latency corrections when merging waveforms from the same event. The time walk curves were fitted for each pad using Equation 4, as explained in Section 1.2.

To improve the stability of the fit, particularly at high dynamic ranges where statistics were poor (due to the lack of fully contained events limited by the size of pads), the baseline offset parameter a was fixed. This offset was determined by calculating the median of the highest 30 % of sorted time difference data, corresponding to the highest signal amplitudes. The high-amplitude region was chosen for its reduced sensitivity to noise, providing a more reliable estimate for the baseline offset.

The correction obtained from the enabled synchronization of signals from different pads, allows for the combination of waveforms from the same event to characterize the overall time resolution of the detector (Figure 24a).

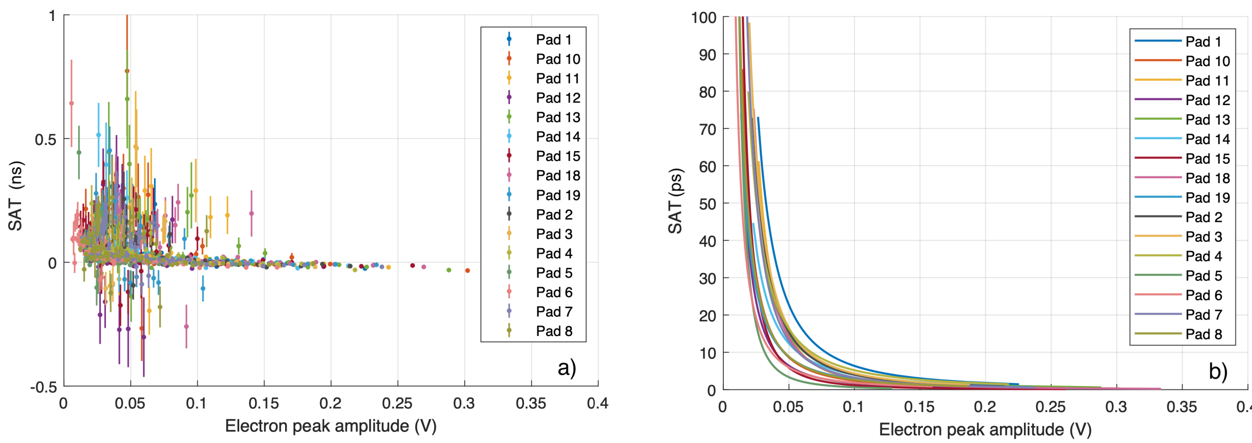

Figure 24: a) Time-walk correction applied to the signal and b) the corrected SAT as a function of electron-peak charge.

After applying the offset correction, the time-walk corrected SAT as a function of the electron-peak charge was fitted (Figure 24b). The combined time resolution for all pads was determined to be 43 ps by weighting the time of each corrected SAT by the signal amplitude.

While individual pads exhibited varying time resolutions, the overall combined resolution remained consistent, not improving the individual pad measurements. This consistency suggests that the fitting procedure for the time-walk correction, particularly the necessity to fix the offset parameter due to low statistics at high charge events, is a primary constraint on the detector's time resolution.

4 Double DLC Multipad

Despite initial R&D efforts using smaller detectors, the ultimate goal is to develop a large-area PICOSEC detector. To this end, the MM board has been scaled up to a 10×10 cm^2 detector with a with one hundred square pads with dimensions of $1\,\text{cm}\times1\,\text{cm}$. Various layout configurations were tested, including non-resistive and single DLC boards [22]. This section introduces a new configuration: the double DLC multi-pad detector (Figure 25), designed to enhance performance, especially in high-rate environments.

Previously, the resistive 10×10 cm^2 PICOSEC detector was grounded by eight connections along its edges (two per side). For improved vertical charge evacuation, the detector now features a double DLC layout. This design includes filled vias [1] in the insulating layer that connect the resistive layers with the readout pads. This configuration offers two significant advantages: firstly, it enhances charge evacuation, which helps maintain a stable electric field even under high particle rates, reducing the impact of fluctuating currents on the applied field; secondly, it provides better protection for the readout electronics by diverting excess current away from the readout pads. This diversion minimizes the risk of voltage drops caused by high currents, ensuring the readout electronics remain protected and operate reliably even in demanding conditions.

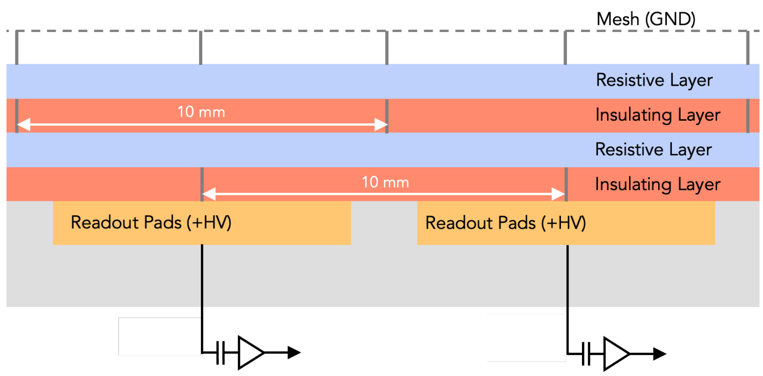

Figure 25: Schematic diagram of the double DLC layout.

To characterize the detector, gain uniformity was measured using the same setup as for the single pad detectors. Each pad was individually illuminated with a UV LED, and the resulting waveforms were collected using a charge-sensitive preamplifier connected to the PCB via the same components to avoid systematic errors.

The detector was tested at various cathode voltages, showing an exponential increase in gain with the cathode voltage. The upper operational limit was found to be 520 V with an anode voltage of 275 V, with first signs of sparks and instabilities observed at 530 V. Gain uniformity was measured at 520 V, and the analysis followed the same procedures as for the single pad detector. Figure 26 displays the mean amplitude uniformity obtained from fitting the Polya function to the SPE amplitude spectra, where the mean is 15.28 mV and the coefficient of variation 8%, ranging from 13.01 mV to 19.10 mV.

[1] Small conductive pathways that pass through an insulating layer to electrically connect different layers within a multilayer structure.

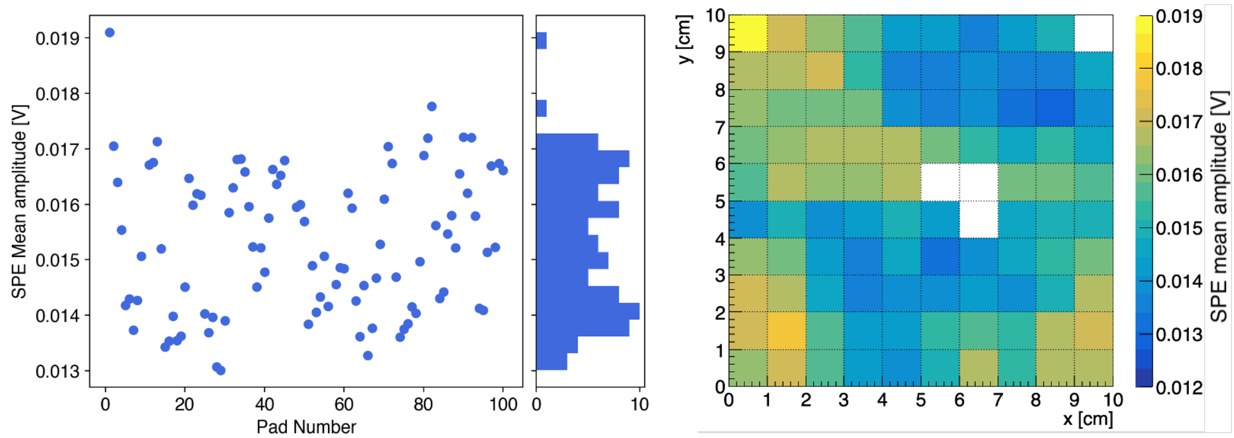

Figure 26: SPE mean amplitude uniformity of the double DLC multi-pad detector at 520 V on the cathode and 275 V is analyzed. The left plot shows the pad number versus the mean amplitude, while the right plot presents the SPE amplitude distribution for each pad in a 2D map.

A preliminary comparison was made to determine if the double DLC multi-pad detector outperforms the single pad detector. The mean amplitude of the SPE for some pads of the single DLC detector was measured, and the results are presented in Figure 27. The mean SPE amplitude was 6.49 mV, with a coefficient of variation of 40%. The amplitudes ranged from 2.91 mV to 13.17 mV, with 520 V applied to the cathode and 275 V to the anode. This preliminary comparison indicates that the double DLC multi-pad detector outperforms the single-pad detector in gain uniformity.

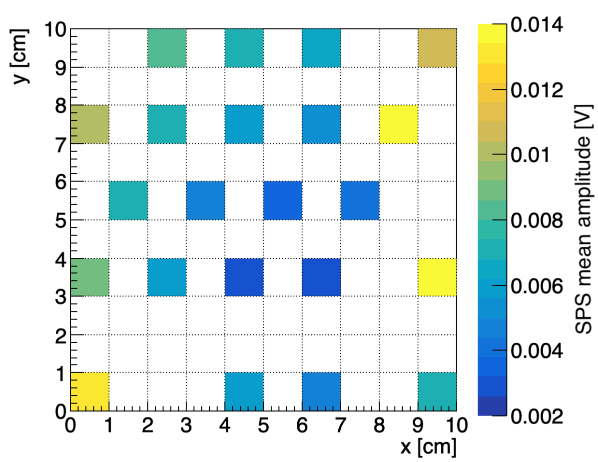

Figure 27: 2D map of the SPE amplitude of the single DLC multi-pad detector at 520 V on the cathode and 275 V on the anode.

Currently, no results are available for time resolution, as the detector has not yet been tested on the beam line. This evaluation is expected to be part of the upcoming test beam campaign.

5 Conclusion

In this work, the performance of various PICOSEC detector prototypes was evaluated using different geometries, including single-pad detectors, medium granularity detectors, and double DLC multi-pad detectors.

The results obtained from the single pad detectors revealed that the standard mesh provided the best performance in terms of gain and time resolution. The limiting factors for the different tested meshes were the transparency in the case of the thin mesh and the uniformity of the field in the case of the electroformed mesh, where wrinkles in the mesh were observed.

The medium granularity detector showed a time resolution of 43 ps and a spatial resolution of 1.31 mm in the x-direction and 1.25 mm in the y-direction. The time resolution was consistent across all pads, suggesting that the fitting procedure for the time-walk correction is a primary constraint on the detector's time resolution as the analysis was limited by the low statistics at high charge events.

Lastly, the double DLC multipad detector was introduced as a new configuration to enhance the detector's performance in high-rate environments. The preliminary results showed that the double DLC multi-pad detector outperforms the single pad detector in terms of gain uniformity, with a mean gain of 15.28 mV and a coefficient of variation of 8%. The time resolution of the double DLC detector has not yet been tested on the beamline, but this evaluation is expected to be part of the upcoming test beam campaign.

Overall, the results obtained from the different detectors provide valuable insights into the performance of the PICOSEC detector and highlight the importance of transparency, uniformity, and time-walk correction in achieving high-precision temporal measurements.

Acknowledgements

First and foremost, I would like to express my sincere gratitude to my supervisors, Dr. F. Brunbauer and M. Lisowska, for their exceptional mentorship and support throughout this project. Their technical expertise and guidance have been invaluable to both my research and personal development during my time at CERN. I would also like to extend my thanks to D. Janssens for the assistance provided with the simulations.

I am also grateful to CERN, the EP-DT-GDD group, and the PICOSEC Collaboration for providing me with this invaluable opportunity. The experience gained through the CERN Summer Student Programme has been truly transformative. Also, thanks to Prof. A. M. Szelc and Prof. J. Monroe for providing the reference letters that enabled my participation in this program.

I also appreciate the friends I made at CERN; their company made this experience unique. Lastly, my heartfelt thanks go to my family for their continuous encouragement and support, os quiero -154.000 y πco.

References

[1] DRD1 Collaboration. *DRD1: Development of Gaseous Detectors Technologies*. Accessed: 2024-07-17. 2024. URL: https://drd1.web.cern.ch.

[2] Hans Geiger. "On the Scattering of α-Particles by Matter". In: *Proceedings of the Royal Society of London A* 81.546 (1908), pp. 174–177. DOI: 10.1098/rspa.1908.0067.

[3] Hans Geiger and Walther Müller. "Electron counting tube for the measurement of the weakest radioactivities". In: *Die Naturwissenschaften* 16.31 (1928), pp. 617–618.

[4] A. Barr et al. "Construction, test and operation in a high intensity beam of a small system of micro-strip gas chambers". In: *Nucl. Instrum. Methods Phys. Res. A* 403 (1998), pp. 31–42.

[5] Y. Giomataris et al. "MICROMEGAS: a high-granularity position-sensitive gaseous detector for high particle-flux environments". In: *Nuclear Instruments and Methods in Physics Research Section A: Accelerators, Spectrometers, Detectors and Associated Equipment* 376.1 (1996), pp. 29–35. DOI: 10.1016/0168-9002(96)00175-1.

[6] Bernd Stelzer. "The New Small Wheel Upgrade Project of the ATLAS Experiment". In: *Nuclear and Particle Physics Proceedings* 273-275 (2016). 37th International Conference on High Energy Physics (ICHEP), pp. 1160–1165. ISSN: 2405-6014. DOI: https://doi.org/10.1016/j.nuclphysbps.2015.09.182. URL: https://www.sciencedirect.com/science/article/pii/S2405601415006719.

[7] CERN PICOSEC Team. *PICOSEC Micromegas Detectors*. https://picosec-mm.web.cern.ch/. Accessed: 2024-08-28. 2024.

[8] F. J. Iguaz et al. "PICOSEC: Charged particle timing at sub-25 picosecond precision with a Micromegas based detector". In: *Nuclear Instruments and Methods in Physics Research Section A* 903 (2018). For the PICOSEC Micromegas Collaboration, pp. 317–325. DOI: 10.1016/j.nima.2018.06.045.

[9] S. Aune et al. "Timing performance of a multi-pad PICOSEC-Micromegas detector prototype". In: *Nuclear Instruments and Methods in Physics Research Section A: Accelerators, Spectrometers, Detectors and Associated Equipment* 993 (2021), p. 165076. ISSN: 0168-9002. DOI: https://doi.org/10.1016/j.nima.2021.165076. URL: https://www.sciencedirect.com/science/article/pii/S0168900221000607.

[10] Lukas Sohl. *PICOSEC-Micromegas developments and performance tests*. RD51 Miniweek Presentation, CERN. Presented on 11.02.2020. Feb. 2020.

[11] Lukas Sohl. "Development of PICOSEC-Micromegas for fast timing in high rate environments". English. NNT: 2020UPASP084. PhD thesis. Université Paris-Saclay, 2020. URL: https://tel.archives-ouvertes.fr/tel-03167728.

[12] A. Utrobicic et al. *Single channel PICOSEC Micromegas detector with improved time resolution*. 2024. arXiv: 2406.05657 [physics.ins-det]. URL: https://arxiv.org/abs/2406.05657.

[13] Caroline A. Schneider, Wayne S. Rasband, and Kevin W. Eliceiri. "NIH Image to ImageJ: 25 Years of Image Analysis". In: *Nature Methods* 9.7 (2012), pp. 671–675. DOI: 10.1038/nmeth.2089.

[14] *COMSOL Multiphysics® v. 6.0 User's Guide*. Available at: https://www.comsol.com. COMSOL AB. 2023.

[15] R. Veenhof. *Garfield++ - Simulation of Gaseous Detectors*. https://garfieldpp.web.cern.ch/garfieldpp/. Accessed: 2024-06-17. 2024.

[16] S. F. Biagi. *Magboltz - Transport of Electrons in Gas Mixtures*. Available at: https://magboltz.web.cern.ch. 2024.

[17] Teledyne LeCroy. *Teledyne LeCroy Oscilloscope Model*. https://www.teledynelecroy.com/oscilloscope/oscilloscopemodel.aspx?modelid=9726. Accessed: 2024-08-29.

[18] Heinz Raether. *Electron Avalanches and Breakdown in Gases*. Butterworths Advanced Physics Series. London: Butterworths, 1964.

[19] R. E. Kalman. "A New Approach to Linear Filtering and Prediction Problems". In: *Journal of Basic Engineering* 82 (1960), pp. 35–45. DOI: 10.1115/1.3662552.

[20] Hamamatsu Photonics. *R3809U High-Speed Photomultiplier Tube*. Accessed: 2024-08-28. 2024. URL: https://www.hamamatsu.com/content/dam/hamamatsu-photonics/sites/documents/99_SALES_LIBRARY/etd/R3809U_TPMH1067E.pdf.

[21] D. Breton et al. "Measurements of timing resolution of ultra-fast silicon detectors with the SAMPIC waveform digitizer". In: *Nuclear Instruments and Methods in Physics Research Section A: Accelerators, Spectrometers, Detectors and Associated Equipment* 835 (2016), pp. 51–60. ISSN: 0168-9002. DOI: https://doi.org/10.1016/j.nima.2016.08.019. URL: https://www.sciencedirect.com/science/article/pii/S0168900216308373.

[22] M. Lisowska et al. "Sub-25 ps timing measurements with 10 × 10 cm2 PICOSEC Micromegas detectors". In: *Nuclear Instruments and Methods in Physics Research Section A: Accelerators, Spectrometers, Detectors and Associated Equipment* 1046 (2023), p. 167687. ISSN: 0168-9002. DOI: https://doi.org/10.1016/j.nima.2022.167687. URL: https://www.sciencedirect.com/science/article/pii/S0168900222009792.

Appendix

A. Simulation

A.1. COMSOL Geometries

Geometries for the various meshes tested in the PICOSEC detector were generated using COMSOL Multiphysics. These geometries were based on mesh dimensions and studied at different voltage configurations. Below are examples of some of these geometries.

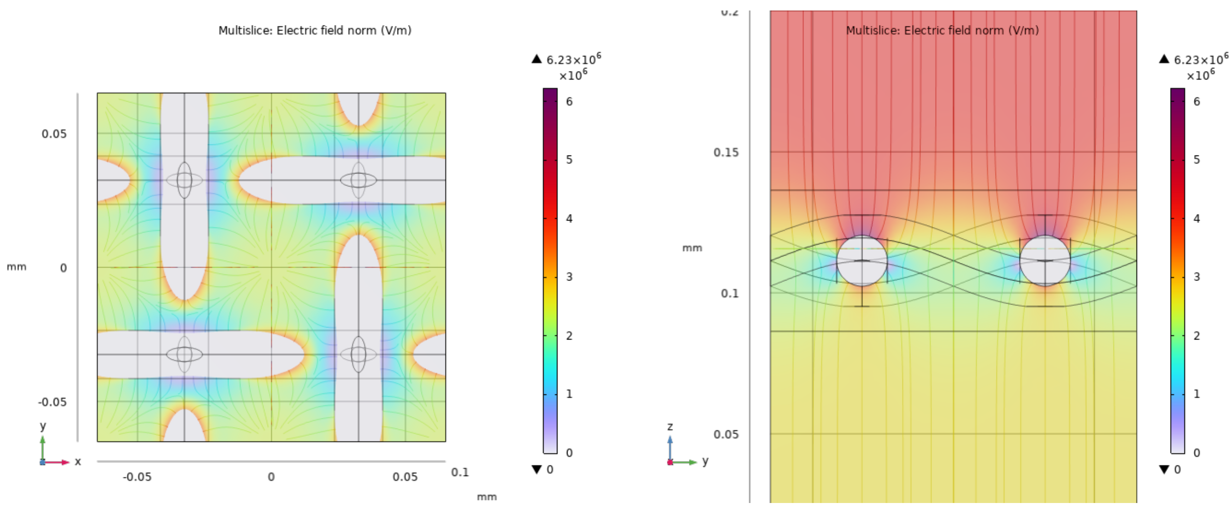

Figure 28: COMSOL MultiPhysics generated electric field for the STD mesh at 275 V on the anode and 475 V on the cathode.

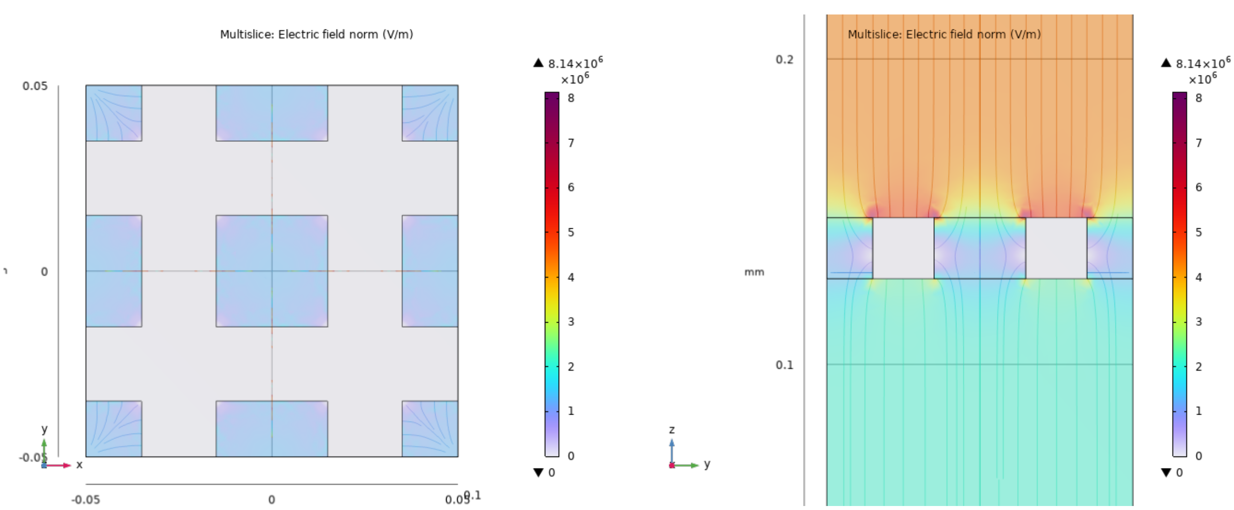

Figure 29: COMSOL MultiPhysics generated electric field for the EF mesh at 275 V on the anode and 500 V on the cathode.

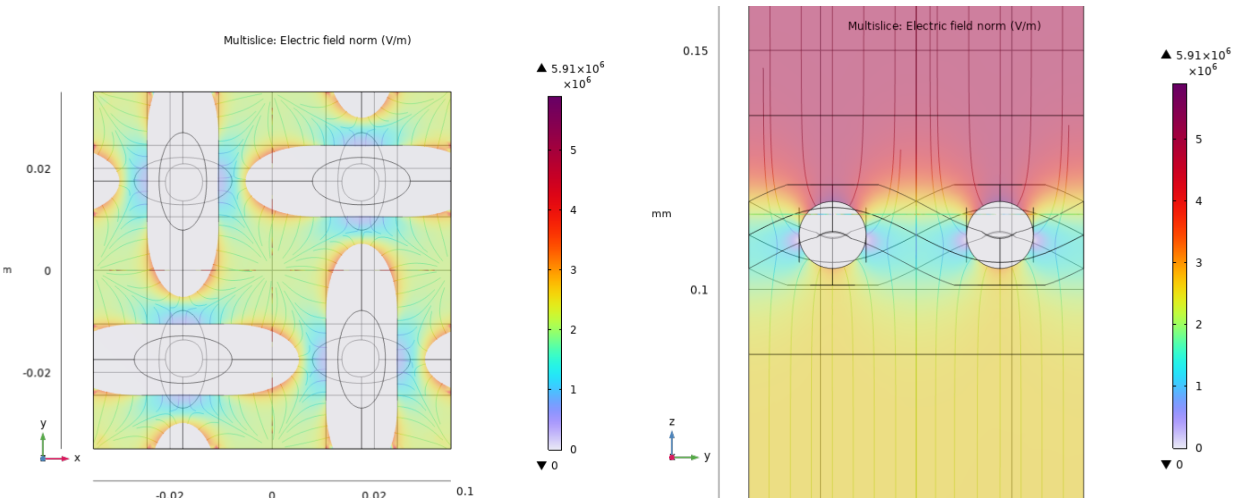

Figure 30: COMSOL MultiPhysics generated electric field for the Thin woven mesh at 275 V on the anode and 560 V on the cathode.

A.2. Signal extraction and theoretical PE spectra

As future work, the amplification factor introduced by the amplifiers and the signal extraction from the detector should be me measured.

To date, only the theoretical PE spectra from the simulation have been obtained from the Garfield++ produced signals, as shown in Figure 31.

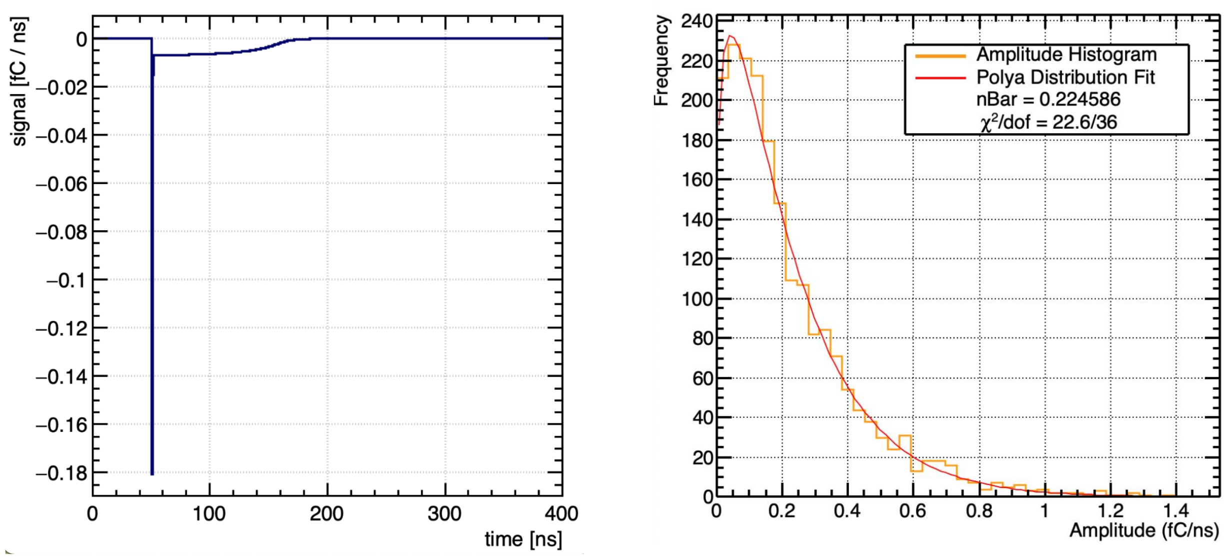

Figure 31: Left: Example of simulated induced signal. Right: Theoretical PE spectra obtained from the Garfield++ simulation for the different meshes.